

Full paper

Core-shell nanostructured organic redox polymer cathodes with superior performance

He Jia^{a,**}, Ting Quan^b, Xuelian Liu^c, Lu Bai^a, Jiande Wang^c, Fadoi Boujioui^a, Ran Ye^d, Alexandru Vlad^c, Yan Lu^{b,e}, Jean-François Gohy^{a,*}

^a Institute of condensed Matter and Nanoscience (IMCN), Bio- and Soft Matter (BSMA), Université catholique de Louvain, Place L. Pasteur, 1, 1348, Louvain-la-Neuve, Belgium

^b Institute for Soft Matter and Functional Materials, Helmholtz-Zentrum Berlin für Materialien und Energie GmbH, Hahn-Meitner-Platz 1, D-14109, Berlin, Germany

^c Institute of condensed Matter and Nanoscience (IMCN), Molecular Chemistry, Materials and Catalysis (MOST), Université catholique de Louvain, Place L. Pasteur 1, 1348, Louvain-la-Neuve, Belgium

^d Institute of Information and Communication Technologies, Electronics and Applied Mathematics (ICTM), Université catholique de Louvain, 1348, Louvain-la-Neuve, Belgium

^e Institute of Chemistry, University of Potsdam, 14467, Potsdam, Germany



ARTICLE INFO

Keywords:

Nanostructured
Redox polymer
Organic electrode
Lithium ion battery
Energy storage

ABSTRACT

Core-shell nanoparticles stabilized by a cationic surfactant are prepared from the poly(2,2,6,6-tetramethylpiperidinyloxy-4-yl methacrylate) redox polymer. The nanoparticles are further self-assembled with negatively charged reduced graphene oxide nanosheets and negatively charged multi-walled carbon nanotubes. This results in the formation of a free-standing cathode with a layered nanostructure and a high content of redox polymer that exhibits 100% utilization of the active substance with a measured capacity as high as 105 mAh/g based on the whole weight of the electrode.

1. Introduction

High-performance lithium-ion batteries currently constitute one of the most investigated energy sources due to the high demand of our modern society for various applications ranging from communication devices, electric and hybrid vehicles, health monitoring devices, the internet of things, etc. [1,2] Compared to inorganic materials, electrodes based on organic active materials attract more and more attention due to their inherent advantages such as renewability, lightness, fast charge and discharge abilities, and more environmentally friendly features, just to name a few [3–7]. Among the different active organic materials investigated so far, poly(2,2,6,6-tetramethylpiperidinyloxy-4-yl methacrylate) (PTMA), a polymer bearing persistent nitroxide radicals in the repeating unit, has become one of the most promising candidates as cathode material for lithium-ion batteries, which exhibits a fast reversible redox reactions and allows high energy storage (111 mAh/g for the one-electron redox reaction and 222 mAh/g for the two-electron redox reaction) [8], high potential (3.6 V vs Li/Li⁺) [9] and a long cycling life [10]. Moreover, the commercial availability of its monomer (2,2,6,6-tetramethylpiperidinyloxy-4-yl methacrylate, TMA)

and of its precursor monomer (2,2,6,6-tetramethylpiperidin-4-yl methacrylate, TMPM) is also an advantage compared to other, less accessible, redox polymers [11].

However, the performances of lithium-ion batteries based on PTMA are greatly hindered by the solubility of PTMA into organic electrolytes and its limited electrical conductivity [12–14]. With the aim of improving the stability and conductivity of PTMA, numerous efforts have been performed. For example, increasing the molar mass [15], cross-linking [16] and grafting onto a solid/rigid substrate [17] can effectively decrease dramatically the solubility of PTMA in organic electrolytes. Forming a copolymer containing an electrically conducting block [18] or anchoring onto the surface of an electrically conducting material [9] are also valuable strategies to increase the performances of PTMA-based electrodes.

Nevertheless, those approaches for the molecular structure modification and for the process of grafting PTMA onto the surface of the functional materials might be cumbersome. Moreover, for most of the methods reported so far, a high content of PTMA leads to the aggregation of the active material in the system, resulting in inefficient electrical connections in and between PTMA particles hampering the

* Corresponding author.

** Corresponding author.

E-mail addresses: he.jia@uclouvain.be (H. Jia), jean-francois.gohy@uclouvain.be (J.-F. Gohy).

whole capacity of PTMA to be utilized during battery operation [19–21]. To overcome this issue, there is still a need for a large amount of carbon conductor to be added and to be intimately mixed in the electrode, although this reduces the specific capacity of the entire electrode due to the limited capacity of the conductive additives.

As the most well-known two-dimensional carbon nanomaterial, graphene has been widely used as functional additive for lithium-ion batteries due to its numerous advantages, such as superior transport rate for lithium ions and electrons, chemical stability, good mechanical strength and high specific surface area [22–24]. Moreover, reduced graphene oxide (rGO) has also been developed for freestanding lithium-ion cathodes, because of its contribution to the capacity originating from the surface Faradaic reaction and the double-layer capacitance [25,26]. In this context, some recent works have presented a combination of PTMA with rGO via chemical modification or physical mixing methods, which will not only improve the conductivity of the composite materials but also contribute to the specific capacity of the entire electrode. For instance, Guo et al. [8] prepared composite cathodes by directly blending PTMA with rGO and proved that two-electron redox reactions of PTMA were observed owing to the addition of rGO.

Zhang et al. [27] and Li et al. [28] successfully synthesized PTMA@rGO hybrid systems by using π - π stacking interactions and surface grafting approaches, respectively. Compared to physical mixing, chemical modification improves the interaction between PTMA and rGO and allows the introduction of more oxygen-containing functional groups on the surface of rGO, hence resulting in an increased loading of PTMA in the composite system and therefore in an increased specific capacity for the whole cathode. However, such grafting approaches and π - π stacking interactions require multiple synthetic steps to modify the rGO surface or the PTMA segments. Furthermore, aggregation of the active material in the system cannot be avoided by the chemical modification approach, thus the effective content of PTMA were only 20 wt % and 22.6 wt %, respectively.

Here we present for the first time the use of PTMA core-shell nanoparticles with a cetyl trimethyl ammonium bromide shell (PTMA@CTAB) as an active component for the preparation of free-standing composite electrodes with functional rGO nanosheets mixed with multi-walled carbon nanotubes (rGO@MWCNT). As depicted in Scheme 1, thanks to the flexibility of rGO nanosheets and the electrostatic interactions between the negatively charged rGO and the positively charged PTMA@CTAB nanoparticles, the latter ones are expected to be dispersed uniformly on the surface of rGO and individually wrapped without aggregation. Thus, the longest path way for the electrons and the ions through the active materials are fixed as the diameter of the PTMA@CTAB nanoparticles, which will improve the utilization of the active materials at high current density. With the assistance of Van der Waals forces between rGO nanosheets and the

bridging connections originating from MWCNTs, free-standing PTMA@CTAB@rGO@MWCNT composite membranes with hierarchical structures are expected to be easily obtained through vacuum filtration.

2. Experimental section

2.1. Materials

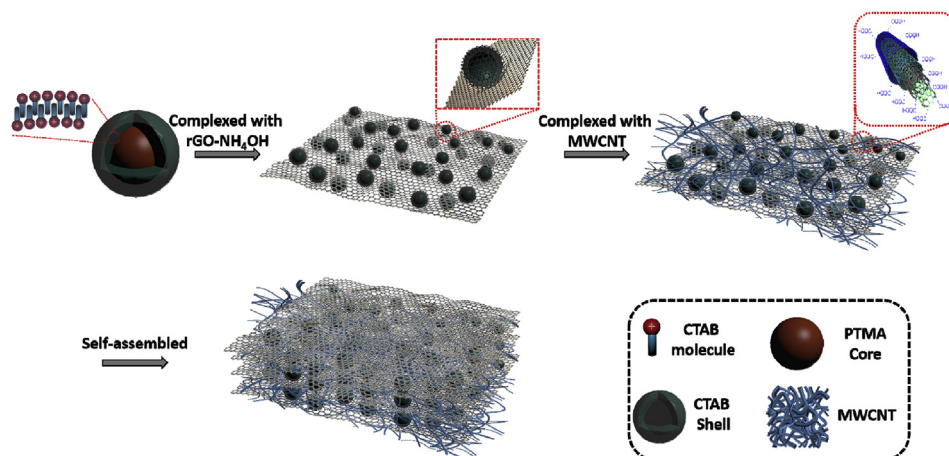
(4-cyano-4-(phenylcarbonothioylthio)pentanoic acid, cetyltrimethylammonium bromide (CTAB), 2,2-Azobis(2-methylpropionitrile) purum (AIBN), $\text{Na}_2\text{WO}_4 \cdot 2\text{H}_2\text{O}$, and hydrazine (35 wt% in H_2O) were supplied by Sigma-Aldrich. 2,2,6,6-tetramethylpiperidin-4-yl methacrylate (TMPPM) was supplied by TCI. Ethylenediaminetetraacetic acid (EDTA) and H_2O_2 (35 wt% in H_2O) were supplied by Acros Organics. Graphene oxide (2 mg/ml water dispersion) (GO) was obtained from XFNANO and water dispersed multi-wall carbon nanotubes (PD15L15-COOH) (MWCNT) was purchased from Nanolab. All of the reactants were used without further purification. Water was purified by a Milli-Q system.

2.2. Synthesis of PTMA

Poly(2,2,6,6-tetramethylpiperidinyloxy-4-yl methacrylate) (PTMA) with controlled molar mass was prepared according to previously reported procedures [29]. Firstly, poly(2,2,6,6-tetramethylpiperidin-4-yl methacrylate) (PTMPM) was synthesized by RAFT polymerization. The monomer (TMPPM: 4 g, 17.75 mol), the chain transfer agent (4-cyano-4-(phenylcarbonothioylthio)pentanoic acid: 77.5 mg, 0.28 mol) and the initiator (AIBN: 45.55 mg, 0.28 mol) were dissolved in 18 ml of ethanol. After complete dissolution, the mixture was placed in an oil bath at 70 °C and the polymerization started immediately. All of the above processes were carried out under argon atmosphere. The product PTMPM was collected by recrystallization and dried overnight in vacuum oven at 40 °C. In the second step, PTMA was prepared by PTMPM oxidation with hydrogen peroxide as follows. To a methanol solution of PTMPM (100 ml, 20 mg/ml), 0.48 g EDTA and 0.71 g $\text{Na}_2\text{WO}_4 \cdot 2\text{H}_2\text{O}$ were added. Then 7.4 ml H_2O_2 (35%) were added and stirred at 60 °C for 48 h. The mixture was filtrated and recrystallized with acetone and hexane. Finally, the orange PTMA product was dried in vacuum overnight.

2.3. Synthesis of PTMA@CTAB core-shell nanoparticles

1.5 ml of PTMA solution (7.4 mg/ml in CHCl_3) were added into 10 ml CTAB aqueous solution (3.75 mg/ml) under vigorous stirring for 1 h at room temperature. After stirring for another 2 h, the mixture was placed in an oil bath at 63 °C to evaporate the chloroform in the



Scheme 1. Schematic illustration of the procedure used to produce PTMA@CTAB@rGO@CNT free-standing cathode materials.

solution. The core-shell nanoparticles were collected by centrifugation and washed with water for 2 times.

2.4. Synthesis of PTMA@CTAB@rGO@MWCNT self-standing electrode

In the first step, water dispersed reduced graphene oxide (rGO) nanosheets were prepared according to the method reported by Wallace's group with minor modifications [30]. 0.85 ml ammonia solution (28 wt% in water) were mixed with 40 ml graphene oxide (GO) aqueous solution (0.25 mg/ml) and stirred for 1 h. Then 20 μ l hydrazine solution (35 wt% in water) were added into the dispersion at 95 °C. The brown dispersion became black after 30 min and the reaction was run for 1 h.

Afterwards, 20 ml of PTMA@CTAB dispersion (0.4 mg/ml) were added into 40 ml of rGO water dispersion (0.25 mg/ml) in 1 h and the mixture was stirred for another 2 h. Then 10 ml of MWCNT (0.1 mg/ml) were mixed with PTMA@CTAB@rGO dispersion for 24 h.

Self-standing electrodes were produced by vacuum filtration of the PTMA@CTAB@rGO@MWCNT aqueous dispersion (0.25 mg/ml) over a nylon 0.2 μ m filter with a millipore set-up, followed by air drying and peeling from the filter. The electrodes were then dried at 40 °C under vacuum for 24 h before electrochemical measurements. The thickness of the composite electrode was 39 μ m and the mass loading of all the components was 2.353 mg/cm².

2.5. Cell assembly

Each electrode, composed of 42.1 wt% PTMA@CTAB core-shell nanospheres (the composition of core-shell nanospheres was 83.3 wt% PTMA and 16.7 wt% CTAB, which equaled 35.07 wt% PTMA and 7.03 wt% CTAB in the composite electrode), 52.6 wt% rGO and 5.3 wt% MWCNT, was tested in half-cell configuration without any additional current collector. A lithium metal foil (99.9% Alfa Aesar) was used as a reference and counter electrode. A glass fiber membrane (Whatman) was used as a separator. The electrolyte consisted of a mixture of ethylene carbonate (EC) and diethyl carbonate (DEC) (1:1 v/v) with 1 M of lithium hexafluorophosphate (LiPF₆ 99.9%, obtained from Solvionic). All cells were assembled under an argon atmosphere (< 0.1 ppm H₂O, < 0.1 ppm O₂) in an MBraun glovebox.

2.6. Characterization

Scanning electron microscope (SEM) images were obtained in a SEM JEOL 7600F. Transmission electron microscope (TEM) images were done with LEO 922. X-ray photoelectron spectroscopy (XPS) analyses were realized at room temperature by using a SSI X-Probe (SSX 100/206) photoelectron spectrometer from FISONS equipped with a monochromatized microfocus Al X-ray source. The electrochemical impedance spectroscopy (EIS) and cyclic voltammetry (CV) tests were carried out using a Parstat 3000. Proton nuclear magnetic resonance (1H NMR) spectra were acquired on a 300 MHz Bruker Avance II. UV-visible spectra were measured by a varian spectro-photometer (Cary, 50 Conc). The galvanostatic charge/discharge tests were performed using a NEWARE battery test system. The zeta-potential was measured by using Malvern Zetasizer Nano ZS ZEN 3500. The hydrodynamic radius of the samples were performed by an ALV/CGS-3 Compact Goniometer System (ALV GmbH, Germany). Thermogravimetric analysis (TGA) was recorded on a TGA/DSC 3 + instrument from Mettler Toledo under air flow with a heating ramp of 10 °C min⁻¹.

3. Results and discussion

Prior to the preparation of the PTMA@CTAB core-shell nanoparticles, linear precursor PTMPM with controlled molar mass was synthesized through controlled reversible addition fragmentation chain

transfer (RAFT) polymerization. As shown in Fig. S1a, the average degree of polymerization (DP) of the obtained PTMPM was 52 as calculated from ¹H NMR. The synthesis was followed by an oxidation reaction of PTMPM into PTMA by using H₂O₂ in the presence of Na₂WO₄·2H₂O and EDTA at 60 °C as catalyst. The conversion of PTMPM into PTMA can be quantified by comparing the UV-vis absorbance of PTMA with the standard curve of the molar absorptivity of the TEMPO radical group which is identical to the nitroxide radical group found in PTMA [31]. As shown in Fig. S1b, the standard calibration curve at 462 nm has been established by measuring the UV-vis absorption of TEMPO in CH₂Cl₂ at different concentrations. After comparing the UV-vis absorbance of the produced PTMA (4.92 mg/ml in CH₂Cl₂) with the standard curve, the conversion of PTMPM into PTMA was determined to be ca. 90%. Thus the calculated average molar mass of the synthesized linear PTMA was 12600 g/mol, a low value which is a benefit for the fabrication of small latex nanoparticles without too many chain physical entanglements. Moreover, since low molar mass linear PTMA shows the less stable in the organic electrolyte [15], it was selected as the cathode materials to test whether the novel designed electrode structure can improve the stability of PTMA.

In the following step, PTMA@CTAB core-shell nanoparticles were synthesized by adding a PTMA dissolved in chloroform into water in the presence of CTAB as surfactant and followed by evaporation of chloroform at 63 °C. As shown in Fig. 1a, uniform PTMA@CTAB core-shell nanoparticles were firstly confirmed by transmission electron microscopy (TEM) measurements and the radius of the spherical particles was around 95 nm which agreed well with the size determined by dynamic light scattering (DLS) at room temperature in water (Fig. s2a). Both of the TEM images and DLS measurements proved the narrow size distribution of the core-shell nanoparticles and a thin layer of CTAB was coated around the PTMA particles as seen from the TEM (inset to Fig. 1a). The amount of available TEMPO radical units of PTMA in the core-shell nanoparticles was quantified to be 75 wt% by comparing the UV-vis absorbance of the PTMA@CTAB CH₂Cl₂ solution with a standard curve as shown in Fig. s2b. The content of CTAB in the core-shell nanoparticles can also be calculated accordingly, which was 16.7 wt%. Thus, the composition of the core-shell particles was 83.3 wt% PTMA (included 75 wt% active units and 8.3 wt% inactive units) and 16.7 wt% CTAB. Due to the large number of positive charges provided by CTAB molecules, the core-shell nanoparticles were well dispersed in water without aggregation as confirmed with a zeta potential value of +80.5 mV.

Water-dispersed reduced graphene oxide (rGO) was synthesized according to a modified reported method [30]. As shown in Fig. s3, the remaining functional groups on the surface of rGO were identified from the C 1s spectra by X-ray photoelectron spectroscopy (XPS). The normalized area related to the C-C peak (at 284.74 eV) was 68.752%, which indicated the reduction of the graphene oxide, a benefit for the increase of the conductivity. Because of the remaining oxygen-containing functional groups (C-O 18.341%, C=O 7.523% and O-C=O 3.568%), the surface of rGO nanosheets is bearing negative charges under high pH conditions (surface zeta potential of rGO: -42 mV), which could make it possible to use a layer-by-layer electrostatic assembly technique to build-up complex systems with the PTMA@CTAB core-shell nanoparticles. The core-shell nanoparticles were mixed with rGO at a mass ratio of 4:5 in water. As shown in Fig. 1b, the core-shell nanoparticles were uniformly attached onto the surface of the rGO nanosheets and coated by them. The coating from rGO not only protected PTMA cores from dissolving into the electrolyte in the following experiments, but also caused the wrinkling of the rGO sheets which increased the surface area of rGO and made the PTMA nanospheres uniformly dispersed in the system without aggregation (as seen in Scheme 1 and Fig. 1b).

In the next step, negatively charged functionalized multi-wall carbon nanotubes (MWCNT-COO⁻) were inserted as the interlayers between each of the PTMA@CTAB@rGO nanosheets (as seen in Scheme

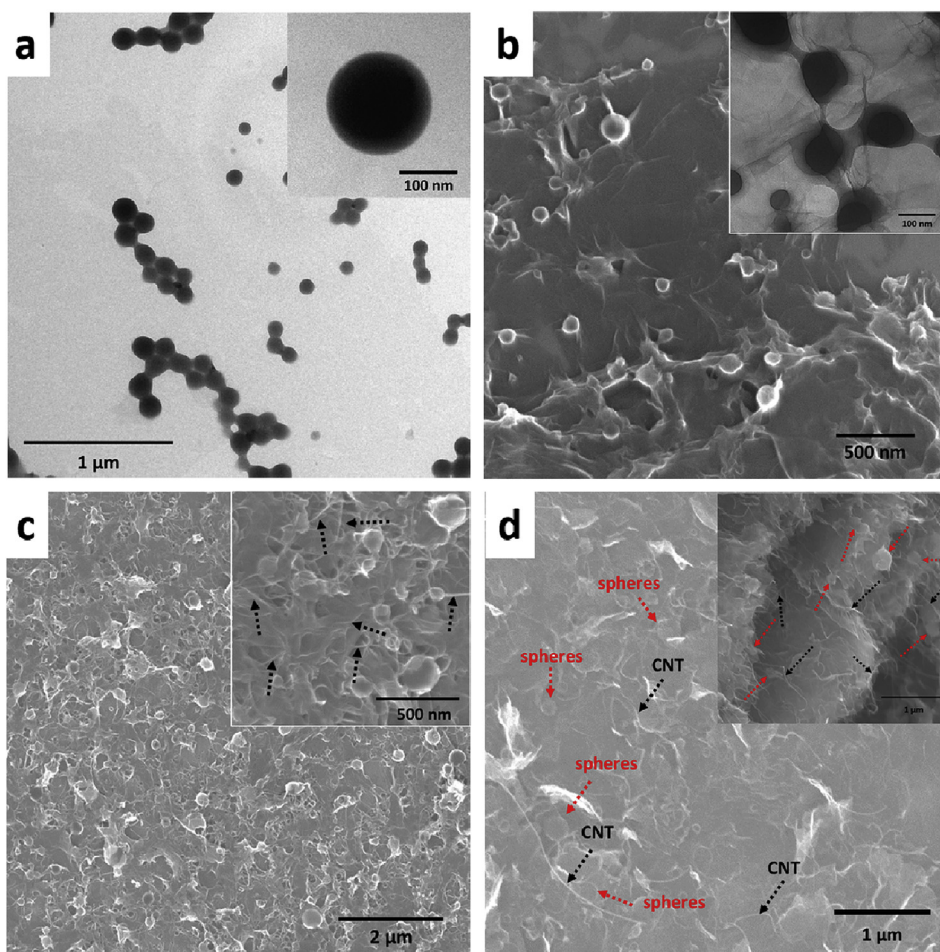


Fig. 1. (a) TEM image of PTMA@CTAB core-shell nanoparticles. (b) SEM and TEM images of PTMA@CTAB@rGO hybrid nanosheets, SEM images of PTMA@CTAB@rGO@MWCNT hybrid nanosheets before (c) and after self-assembly (d), and the cross section of PTMA@CTAB@rGO@MWCNT free standing cathode (inset image in d).

1). As shown in Fig. 1c, MWCNTs were homogeneously dispersed on the surface of the hybrid nanosheets, parts of which have been marked with dotted arrows in the inserted focused SEM image. Interestingly enough, owing to the electrostatic interactions and Van der Waals force operating in the system, the self-assembly of the hybrid nanosheets as depicted in Scheme 1 had already taken place during the drying process for the scanning electron microscopy (SEM) sample preparation, which led to a denser particle distribution than in the case of the PTMA@CTAB@rGO nanosheets shown in Fig. 1b. Hierarchical structures in the as-prepared PTMA@CTAB@rGO@MWCNT were finally achieved through simple vacuum filtration of the mixtures (Scheme 1), which yielded self-standing and binder-free hybrid membranes. As shown in Fig. 1d, the surface of the self-assembled membrane was intact and the folding of the rGO nanosheets due to the complexation can be observed clearly. Uniformly distributed PTMA@CTAB nanospheres and MWCNTs have been indeed observed in Fig. 1d. Parts of them are marked with arrows in Fig. 1d. The insert in Fig. 1d shows a cross-section SEM image of the same membrane and reveals multi-layered structures consisting of parallel rGO sheets with uniformly intercalated PTMA@CTAB core-shell nanospheres and functionalized MWCNTs. In summary, the results depicted in Fig. 1 confirm the hypothesized structures in Scheme 1 for our PTMA@CTAB@rGO@MWCNT hybrid electrode. The next step is to investigate those free-standing membranes as cathodes for Li-ion batteries.

Electrochemical measurements were performed in the half-cell configuration by using lithium metal as negative electrode and the PTMA@CTAB@rGO@MWCNT composite film as positive electrode.

Thanks to the freestanding nature of the hybrid films, no additional current collectors were needed, and the weight of the cathode was accordingly greatly reduced. The composition of the electrode was confirmed by TGA measurements (see Fig. s6), which was almost identical to the initial ratio of the different components.

The galvanostatic charge/discharge measurements at different current densities and normalized to the weight of PTMA were carried out within a voltage window of 3.0–4.0 V (vs Li/Li⁺). As shown in Fig. 2a, the electrode of PTMA@CTAB@rGO@MWCNT composite film exhibited a high reversible capacity up to 140 mAh/g based on the content of PTMA active units at 0.2C current density, which was much higher than the theoretical value of PTMA (111 mAh/g). Even at 4C current density, the specific capacity of the hybrid films approached 100 mAh/g. Such a high reversible capacity can be attributed to the following reasons.

Firstly, the rGO@MWCNT additives (57.9 wt% in the composite electrode) also contribute in part to the capacity (see Table 1). As shown in Fig. 2c, the cyclic voltammetry (CV) analysis of the composite cathode was explored over the potential window ranging from 3.0 to 4.0 V. A set of symmetrical redox peaks were found at 3.5–3.7 V (vs Li/Li⁺) corresponding to the typical voltage plateau of PTMA at 3.6 V in the charge-discharge curves (see Fig. 2a), which can be explained by the redox reactions of the PTMA nitroxide radicals and the oxoammonium cations. In addition to the pair of redox peaks from PTMA, a rectangular CV shape was also noted in Fig. 2c that could be associated to the slope-shaped curve before and after the plateau in Fig. 2a. This characteristic feature is typical of the rGO capacitive behavior (see

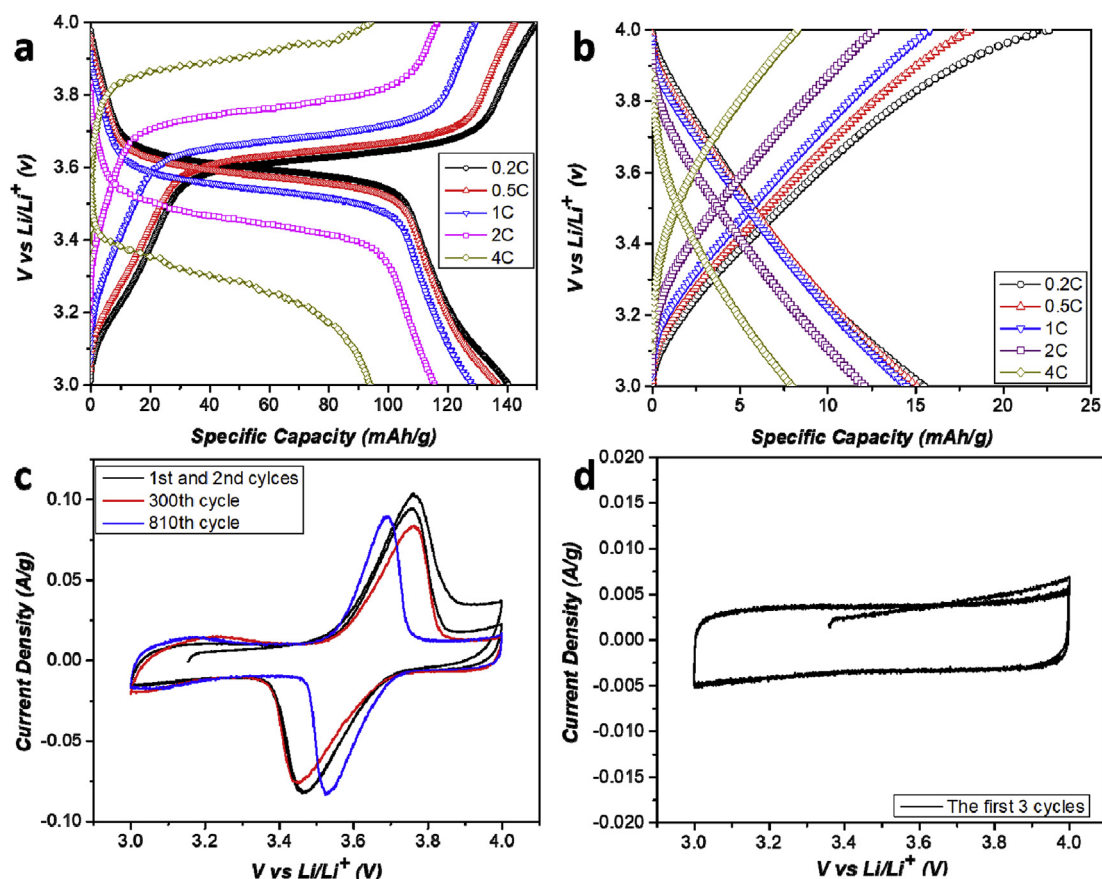


Fig. 2. Charge/discharge curves of (a) PTMA@CTAB@rGO@MWCNT and (b) rGO@MWCNT at different C rates (1C = 111 mA g^{-1}). (c) Cyclic voltammogram curves of PTMA@CTAB@rGO@MWCNT with the initial two (black), the 300th (red) and the 810th (blue) scans (0.05 mV/s). (d) Cyclic voltammogram curves of rGO@MWCNT with the initial three scans (0.05 mV/s). All the electrochemical measurements were performed in the 3 V–4 V voltage range. (For interpretation of the references to colour in this figure legend, the reader is referred to the Web version of this article.)

Table 1

The specific capacities of different components in the composite cathodes at different current densities.^a

Current density	C _{total} ^b (mAh/g)	C _{rGO@MWCNT} ^c (mAh/g)	C _{rGO@MWCNT} ^d (mAh/g)	C _{PTMA} ^e (mAh/g)
0.2C	140.5	15.5	9	112
0.5C	137.1	15.1	8.7	109.5
1C	128.4	14.4	8.4	101.9
2C	115.7	12.1	7	93.7
4C	94	8	4.6	79.4

^a The composition of the cathode materials was 42.1 wt% PTMA@CTAB nanospheres (included 31.6 wt% active units of PTMA, 3.47 wt% inactive units of PTMA and 7.03 wt% CTAB), 52.6 wt% rGO and 5.3 wt% MWCNT.

^b The total specific capacity based on PTMA active materials.

^c The theoretical specific capacity of rGO@MWCNT according to the measurement in Fig. 2d.

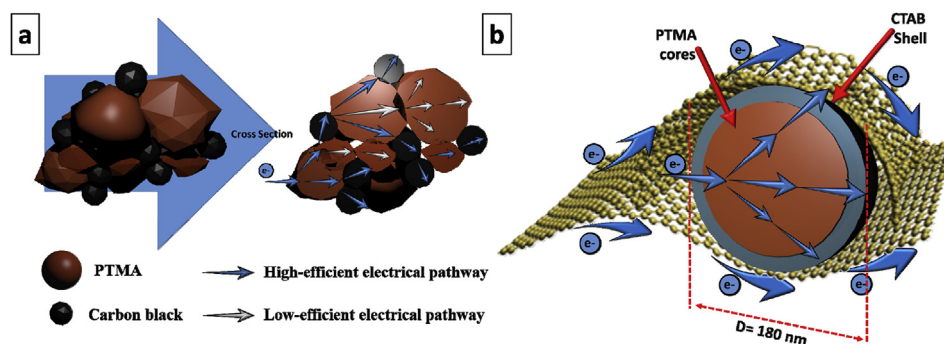
^d The specific capacity contribution of rGO@MWCNT in the hybrid cathode materials.

^e The specific capacity contribution of PTMA in the hybrid cathode materials, which was calculated based on the active units of PTMA.

the CV profile of rGO@CNT in Fig. 2d and the slope of rGO@CNT curves in Fig. 2b). Thus, the high specific capacity of the investigated PTMA@CTAB@rGO@MWCNT composite film mainly consists of two parts: the redox reactions associated to PTMA and the capacitance related to rGO. The capacitance of rGO is mainly attributed to double-layer capacitance at the potential window ranged from 3.0 to 4.0 V.

The second reason to explain the outstanding performances of our hybrid electrodes is related to their structure. Indeed, our composite

PTMA@CTAB@rGO@MWCNT electrodes consist of uniformly distributed PTMA nanospheres wrapped by rGO, avoiding aggregation of the active material and shortening transport pathways of ions and electrons. Thereby, excellent contact between PTMA and rGO@MWCNT additives is achieved and the effective capacity of PTMA in the system is increased. As depicted in Scheme 2a, the use of ill-defined PTMA particles with carbon black particles may lead to the aggregation of PTMA, especially at high PTMA mass loading. In this scenario, the pathways of electrons and ions in the active material could be extremely prolonged. Since PTMA is essentially an electrically insulating material, inefficient electrical connections between PTMA particles are generated resulting in poor electrochemical performances. Moreover, some buried PTMA area could not be available for redox reactions, decreasing the capacity of the electrode. On the contrary, in the PTMA@CTAB@rGO@MWCNT composite electrode, PTMA@CTAB nanospheres are wrapped by rGO without aggregation even at a content as high as 42.1 wt% (included 35.07 wt% PTMA and 7.03 wt% CTAB, see Fig. 1b and Scheme 2b). Therefore the longest transport distance of ions and electrons in the active material is fixed by the diameter of the PTMA nanospheres, which is only 180 nm (see Scheme 2b). In comparison to the ill-defined system depicted in Scheme 2a, the optimized PTMA@CTAB@rGO@MWCNT structure investigated in the present study allows efficient utilization of PTMA. As shown in Fig. s7, electrodes containing a higher ratio of PTMA@CTAB nanospheres have also been synthesized. However, when the content of nanospheres was increased from 42.1 wt% to 54 wt%, the electrode plate was broken, which is believed to result from the increased number of electrostatic interactions between PTMA@CTAB nanospheres and rGO sheets overwhelming the Van der Waals forces between each of the rGO sheets.



Scheme 2. Schematic diagram of the electron-transport path for (a) bare-PTMA with carbon black as conductive additive and (b) PTMA@CTAB@rGO@MWCNT hybrid cathode materials.

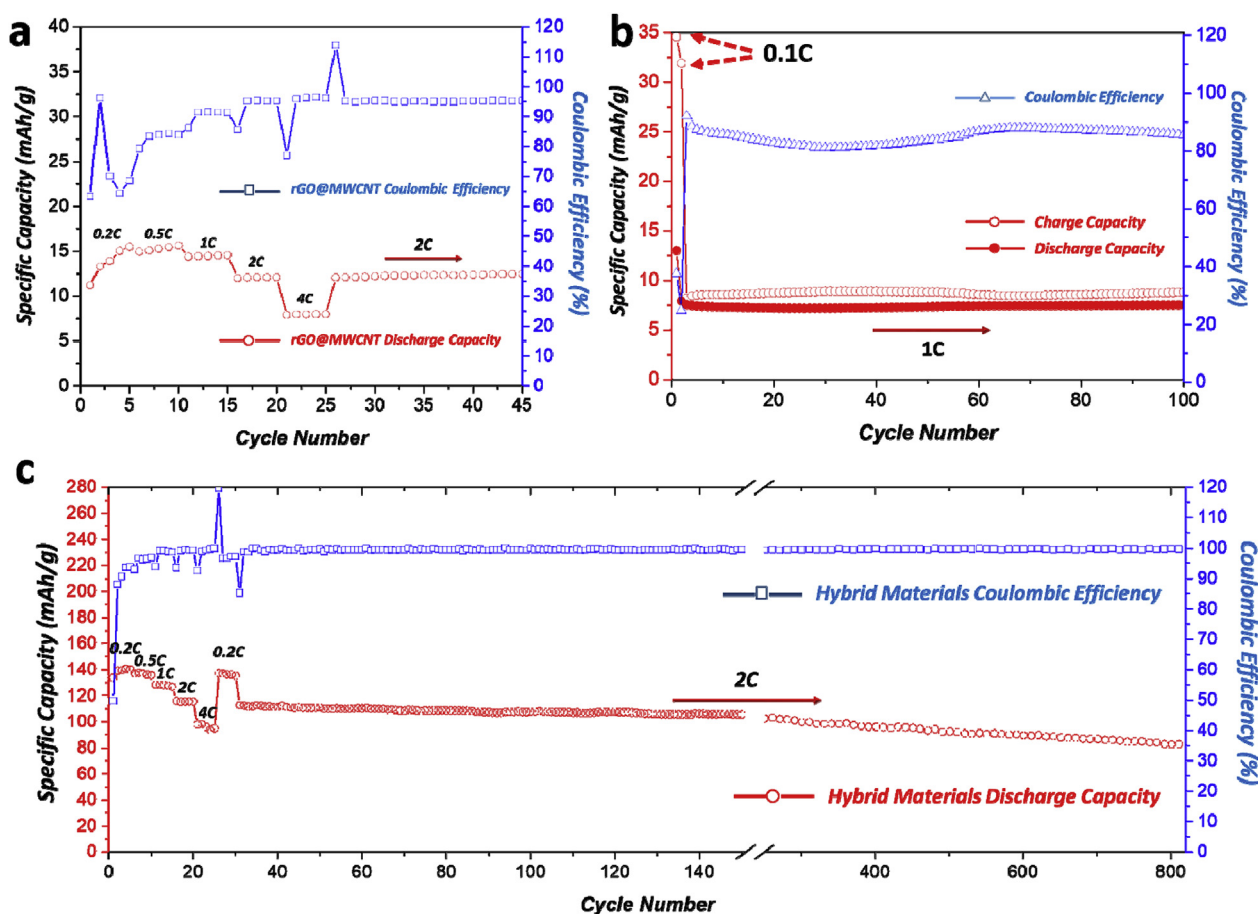


Fig. 3. (a) Cycle performance of rGO@MWCNT at various current rates. (b) Cycle performance of bare PTMA at 1C (the first two cycles were performed at 0.1C) between 3V and 4V voltage range. (c) Electrochemical performance of PTMA@CTAB@rGO@MWCNT at various current rates between 3V and 4V and followed by cycle performance at 2C over 780 cycles. (The current rates for the measurements are identified according to the theoretical capacity of PTMA.)

The specific capacities of rGO@MWCNT and PTMA@CTAB@rGO@MWCNT composite electrodes at various C rates were measured (see Fig. 3a and c) and the specific capacity resulting from PTMA active units in the composite systems could be calculated accordingly. As shown in Table 1, taking the theoretical capacity of PTMA as a reference (111 mAh/g), the calculated specific capacity utilization of PTMA in the hybrid systems reached 100% at 0.2C and 0.5C rates. At rates of 1C and 2C, this efficiency approached 93% and 86%, respectively. Even at 4C, almost 73% of PTMA were utilized in the hybrid system. In the case of a high mass loading in active material, such a high efficiency was difficult to achieve in previous researches on PTMA [8,27,28].

The rate capabilities and charge-discharge cycling performances of

free-standing PTMA@CTAB@rGO@MWCNT composite electrodes were measured by cycling the electrodes at various current densities from 0.2C to 4C followed by 780 cycles at a current density of 2C (Fig. 3c). The discharge specific capacities of the composite electrodes were 140.5, 137.1, 128.4, 115.7 and 94 mAh/g at current densities of 0.2C, 0.5C, 1C, 2C and 4C, respectively. When the current was restored to 0.2C, the composite electrode can still deliver a reversible capacity of 137.3 mAh/g, corresponding to 97.7% of the initial capacity and suggesting very good rate capability. In order to investigate the long cycling performances of the composite electrodes, the measurements were continued at 2C for 780 cycles as shown in Fig. 3c. After 780 cycles, the reversible capacity of the composite electrode remained at 83 mAh/g, corresponding to 74.1% retention of the starting capacity of the cycling

measurement (i.e. 112 mAh/g at the 31st cycle). It means that there is only 0.03% loss of the capacity per cycle for the composite electrodes. Moreover, the Coulombic efficiency remained around 100% for the entire cycling measurement, which indicated excellent capacity retention. As shown in Fig. 2c, the set of typical symmetrical redox peaks of PTMA were clearly observed after 300 and 810 cycles with no change in intensity, which indicated that almost no polymer dissolved into the electrolyte during cycling. In sharp contrast, the slurry consisting of bare PTMA, carbon black and PVDF and coated on the current collector presented a very poor cycling performance (see data plotted in Fig. 3b). It is clear that the smaller its molar mass, the more easily the PTMA is dissolved into the electrolyte. Owing to the quite low molar mass (12600 g/mol) and the longer pathways for ions and electrons (see scheme 2a), the bare PTMA electrode (with 35 wt% of PTMA same as the PTMA@CTAB@rGO@MWCNT composite electrode) only delivered a specific capacity of 7 mAh/g after 100 cycles at 1C, which is 6.4% of the theoretical capacity of PTMA. Even the initial specific capacity of the bare PTMA electrode at a current density of 0.1C was only 35 mAh/g and the Coulombic efficiency was always less than 90% during the cycling (Fig. 3b). The composite electrode without CTAB was also prepared by filtration of the NMP dispersion of PTMA, rGO and MWCNT with the same composition as the PTMA@CTAB@rGO@MWCNT electrode. As shown in Fig. s8, the specific capacity of the composite electrode was only 35.22 mAh/g (the capacity contribution from rGO@MWCNT was also taken account). The reason for this low specific capacity may be that, without CTAB modification, PTMA is no longer protected by the rGO coating and the interaction between PTMA and rGO is not sufficient to stabilize the load of PTMA [8].

The capacities measured for the composite films were found to be highly potential-dependent. As shown in Fig. 4c, when the voltage range was extended from 2 V to 4 V, the reversible capacity of the composite films was increased to 261.6 mAh/g at a current density of 0.2C (to be compared to 140.5 mAh/g at 0.2C when the measurement was performed between 3 and 4 V). Even at 4C current density, the specific capacity of the composite films was still 163.4 mAh/g. Due to the characteristic features of the PTMA@CTAB@rGO@MWCNT composite films, the specific capacity was 105 mAh/g at 0.1C current density when it was normalized to the mass of the whole cathode, which is almost the highest reported value for the PTMA-based cathode materials. Such a substantial increase of the capacity of the composite films can be attributed to the following reasons.

Firstly, PTMA exhibits two-electron redox reactions within the 2–4 V voltage range. As shown in Fig. 4a, two pairs of reversible redox peaks were observed in the CV curves of PTMA@CTAB@rGO@MWCNT composite electrodes between 2.0 and 4.0 V at a scan rate of 0.05 mV/s. In addition to the pair of peaks at around 3.6 V as corresponding to the redox reactions of PTMA radicals and oxoammonium cations, another pair of peaks in the range of 2.7–3.1 V has been observed, which is attributed to the redox reactions associated to PTMA radicals and aminoxyl anions as reported by Guo et al. [8] (see Fig. s5) and cannot be found when the composite electrode was cycled between a narrow voltage range (see Fig. 2c). Two voltage plateaus at 3.1 V and 3.6 V in the charge-discharge curves in Fig. 4c and d also confirm the two-electron redox reaction from PTMA.

A second reason for the increase in capacity for the composite electrodes could be linked to the surface capacitive effect of the rGO@

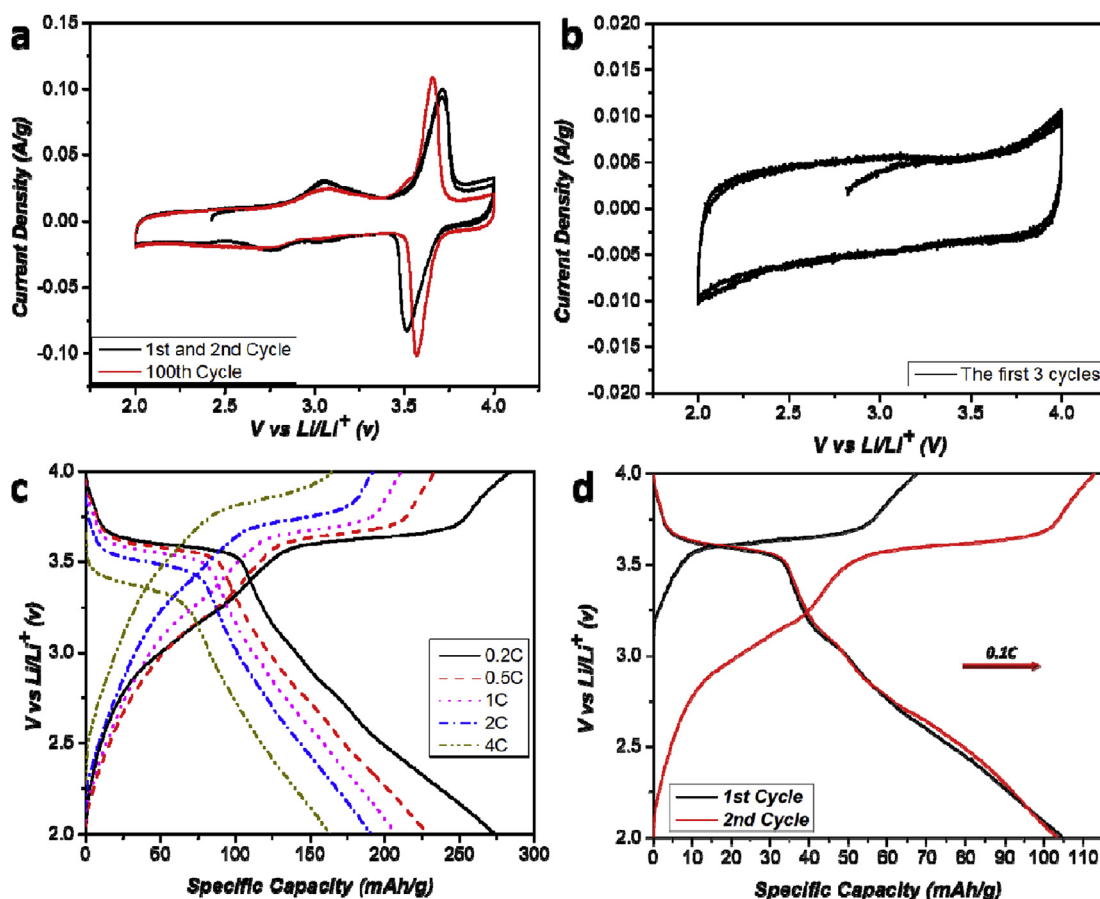


Fig. 4. (a) Cyclic voltammograms curves of PTMA@CTAB@rGO@MWCNT with the initial two and the 100th scan (0.05 mV/s). (b) Cyclic voltammogram curves of rGO@MWCNT with the initial three scans (0.05 mV/s). (c) Charge/discharge curves of PTMA@CTAB@rGO@MWCNT at different C rates. (d) Galvanostatic charge/discharge behaviors of PTMA@CTAB@rGO@MWCNT when normalized to the whole electrode weight with two cycles at 0.1C. All of the electrochemical measurements were performed in the 2–4 V voltage range.

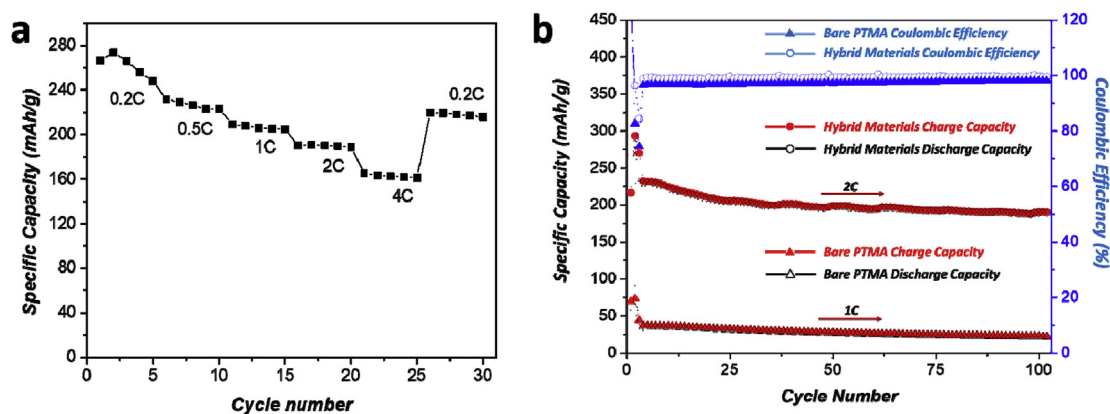


Fig. 5. (a) Electrochemical performances of PTMA@CTAB@rGO@MWCNT hybrid electrodes at various current rates in the 2–4 V voltage range. (b) Cycle performance of PTMA@CTAB@rGO@MWCNT at 2C and bare PTMA at 1C (the first two cycles were performed at 0.2C and 0.1C respectively) in the 2–4 V voltage range over 100 cycles.

MWCNT additives. Due to the chemical reduction of graphene oxide performed in this work, a large number of oxygen-containing functional groups were kept on the surface of rGO (see Fig. s3), which can be electrochemically reduced by Li^+ ions and oxidized reversibly below and above 3.0 V (vs Li/Li^+). As shown in Figs. 4b and 2d, when the lower limit of the voltage range was expanded from 3.0 V to 2.0 V, a higher gravimetric current was observed in the CV curves of the rGO@MWCNT electrode, which is the signature of the Faradaic reactions between the oxygen-containing functional groups and lithium according to previously published literature [26].

In summary, when the PTMA@CTAB@rGO@MWCNT composite electrodes were cycled between 2.0 and 4.0 V, the measured capacity was mainly consisting of the following four parts: the first and the second pairs of electron related to the two redox reactions in PTMA, the Faradaic surface reactions and the double layer capacitance of the rGO@MWCNT additives.

The rate capability of the composite film electrodes in the voltage range from 2.0 to 4.0 V was measured by cycling the electrodes at different current densities based on the weight of PTMA. As shown in Fig. 5a, the discharge specific capacities of the composite electrodes were 261.6, 226.2, 206.6, 190 and 163.4 mAh/g at current densities of 0.2C, 0.5C, 1C, 2C and 4C, respectively. When the cathode was discharged again at 0.2C, around 83.9% of the initial capacity was retained, indicating exceptional rate performances. The cycling performance of the composite cathode at a rate of 2C was demonstrated in Fig. 5b. After 100 cycles, the reversible capacity of the composite electrode remains at 189.6 mAh/g, which means 0.16% capacity loss per cycle. Moreover, maintaining 100% Coulombic efficiency throughout the entire cycling process suggested excellent capacity retention. As shown in Fig. 4a, after 100 cycles, two sets of typical symmetrical redox peaks in the CV curves of the composite electrodes were still clearly observed in agreement with a very good stability of the composite films in the electrolyte. The narrowing of the offset between the oxidation and the reduction peaks after cycling is again attributed to the improvement of the conductivity in the system (see Fig. s4b). Compared to the composite electrodes cycled within a narrow voltage range (3.0 V–4.0 V), this effect was more pronounced. As a comparison, the bare PTMA electrode was cycled at the rate of 1C within the same voltage range. As shown in Fig. 5b, without the modification with rGO, the initial reversible capacity of the bare PTMA electrode was only 35.5 mAh/g. After 100 cycles, the specific capacity was decreased to 21.8 mAh/g, which was only 11.4% of the capacity of composite film electrodes cycled in the same period. Those results demonstrated again the importance of the morphology of the PTMA@CTAB@rGO@MWCNT hybrid electrodes on the electrochemical performances.

4. Conclusion

In this contribution, we have disclosed the preparation of free standing PTMA@CTAB@rGO@MWCNT composite electrodes with electrochemical properties outperforming previous PTMA-based electrodes. Our strategy is based on the use of PTMA core-shell nanospheres with a cetyl trimethyl ammonium bromide shell (PTMA@CTAB) as an active component for the preparation of free-standing composite electrodes with functional rGO nanosheets mixed with multi-walled carbon nanotubes (rGO@MWCNT). With the help of electrostatic interactions and Van der Waals forces operating in and between the negatively charged rGO and the positively charged PTMA@CTAB nanospheres, self-assembled layered structures have been obtained, in which PTMA@CTAB nanospheres are well-dispersed, show no aggregation, are wrapped by rGO and bridged by MWCNTs. Moreover, with the protection of rGO shells, the stability of PTMA in the organic electrolyte is significantly improved and long cycling life has been measured with only 0.03% capacity loss per cycle. At the same time, the uniform dispersion of the nanospheres in the hybrid system leads to a high content of PTMA (35 wt% of PTMA corresponding to 31.6 wt% of active units in this work) accompanied with around 100% of active substance utilization. Most importantly, when the cycling voltage range was extended from 2 V to 4 V, the composite electrodes show almost the highest specific capacity (105 mAh/g) reported so far for PTMA-based electrodes when normalized to the mass of the whole cathode (no need to consider the quality of the current collector due to the free-standing characteristics) owing to the utilization of Faradaic surface reaction of rGO and the second electron redox reaction of the nitroxide radicals in PTMA to aminoxyl anions. Finally, the entire self-assembly process of the composite membrane is carried out in water without polluting the environment and the presented approach can be easily extended to other active polymers.

Conflicts of interest

The authors declare no competing financial interest.

Acknowledgements

HJ and JFG are grateful to the Service Public de Wallonie (SPW-DG06) for funding in the frame of the Programme d'Excellence BATWAL (1318146) and to the CfB for funding in the frame of the Concerted Research Action BATTAB (14/19-057).

Appendix A. Supplementary data

Supplementary data to this article can be found online at <https://doi.org/10.1016/j.nanoen.2019.103949>.

References

- [1] N. Nitta, F. Wu, J.T. Lee, G. Yushin, *Biochem. Pharmacol.* 18 (2015) 252–264.
- [2] Q. Wang, L. Jiang, Y. Yu, J. Sun, *Nano Energy* 55 (2019) 93–114.
- [3] S. Lee, G. Kwon, K. Ku, K. Yoon, S. Jung, H. Lim, K. Kang, *Adv. Mater.* 42 (2018) 1704682.
- [4] D. Larcher, J.M. Tarascon, *Nat. Chem.* 7 (2015) 19.
- [5] P. Poizot, F. Dolhem, *Energy Environ. Sci.* 4 (2011) 2003.
- [6] H. Tokue, T. Murata, H. Agatsuma, H. Nishide, K. Oyaizu, *Macromolecules* 50 (2017) 1950–1958.
- [7] Y. Jing, Y. Liang, S. Gheyhani, Y. Yao, *Nano Energy* 37 (2017) 46–52.
- [8] W. Guo, Y.-X. Yin, S. Xin, Y.-G. Guo, L.-J. Wan, *Energy Environ. Sci.* 5 (2012) 5221–5225.
- [9] B. Ernoult, M. Devos, J.-P. Bourgeois, J. Rolland, A. Vlad, J.-F. Gohy, *J. Mater. Chem. A* 3 (2015) 8832–8839.
- [10] A. Vlad, N. Singh, J. Rolland, S. Melinte, P.M. Ajayan, J.-F. Gohy, *Sci. Rep.* 4 (2014) 4315.
- [11] T. Suga, Y.J. Pu, S. Kasatori, H. Nishide, *Macromolecules* 40 (2007) 3167–3173.
- [12] H. Nishide, T. Suga, *Electrochem. Soc. Interfac.* 14 (2005) 32–36.
- [13] T. Janoschka, M.D. Hager, U.S. Schubert, *Adv. Mater.* 48 (2012) 6397–6409.
- [14] Y. Zhang, A. Park, A. Cintora, S.R. McMillan, N.J. Harmon, A. Moehle, M.E. Flatté, G.D. Fuchs, C.K. Ober, *J. Mater. Chem. C* 6 (2017) 111–118.
- [15] K. Zhang, Y. Hu, L. Wang, J. Fan, M.J. Monteiro, Z. Jia, *Polym. Chem.* 8 (2017) 1815–1823.
- [16] S. Iwasa, T. Nishi, S. Nakamura, *J. Electroanal. Chem.* 805 (2017) 171.
- [17] H.C. Lin, C.C. Li, J.T. Lee, *J. Power Sources* 196 (2011) 8098–8103.
- [18] T. Sukegawa, K. Sato, K. Oyaizu, H. Nishide, *RSC Adv.* 5 (2015) 15448–15452.
- [19] Y. Hu, K. Zhang, H. Hu, S. Wang, D. Ye, M.J. Monteiro, Z. Jia, L. Wang, *Mater. Chem. Front.* 2 (2018) 1805–1810.
- [20] R. Cao, J. Qian, J. Zhang, W. Xu, *Organic cathode materials for rechargeable batteries*, in: Z. Zhang, S. Zhang (Eds.), *Rechargeable Batteries. Green Energy and Technology*, Springer International Publishing., 2015, pp. 637–671.
- [21] Y. Zhang, A.M. Park, S.R. Mcmillan, N.J. Harmon, M.E. Flatte, G.D. Fuchs, C.K. Ober, *Chem. Mater.* 30 (2018) 4799–4807.
- [22] R. Fang, K. Chen, L. Yin, Z. Sun, F. Li, H. Cheng, *Adv. Mater.* 9 (2019) 1800863.
- [23] L. Yan, J. Liu, Q. Wang, M. Sun, Z. Jiang, C. Liang, F. Pan, Z. Lin, *ACS Appl. Mater. Interfaces* 9 (2017) 38159–38164.
- [24] P. Wu, H. Wang, Y. Tang, Y. Zhou, T. Lu, *ACS Appl. Mater. Interfaces* 6 (2014) 3546–3552.
- [25] S.H. Ha, Y.S. Jeong, Y.J. Lee, *ACS Appl. Mater. Interfaces* 5 (2013) 12295–12303.
- [26] H.R. Byon, B.M. Gallant, S.W. Lee, Y. Shao-Horn, *Adv. Funct. Mater.* 23 (2013) 1037–1045.
- [27] K. Zhang, Y. Hu, L. Wang, M.J. Monteiro, Z. Jia, *ACS Appl. Mater. Interfaces* 9 (2017) 34900–34908.
- [28] Y. Li, Z. Jian, M. Lang, C. Zhang, X. Huang, *ACS Appl. Mater. Interfaces* 8 (2016) 17352–17359.
- [29] T. Janoschka, A. Teichler, A. Krieg, M.D. Hager, U.S. Schubert, *Polym. Chem.* 50 (2012) 1394–1407.
- [30] D. Li, M.B. Müller, S. Gilje, R.B. Kaner, G.G. Wallace, *Nat. Nanotechnol.* 3 (2008) 101–105.
- [31] O. Bertrand, B. Ernoult, F. Boujioui, A. Vlad, J.-F. Gohy, *Polym. Chem.* 6 (2015) 6067.